PHYSICAL REVIEW C **93**, 054312 (2016)

Pseudospin-orbit splitting and its consequences for the central depression in nuclear density

Jia Jie Li (李佳杰),[1,2,3] Wen Hui Long (龙文辉),[1,4,*] Jun Ling Song (宋军领),[1,4] and Qiang Zhao (赵强)[1,4]
[1] *School of Nuclear Science and Technology, Lanzhou University, Lanzhou 730000, China*
[2] *Institut de Physique Nucléaire, IN2P3-CNRS, Université Paris-Sud, F-91406 Orsay, France*
[3] *Institut de Physique Nucléaire de Lyon, IN2P3-CNRS, Université de Lyon, F-69622 Villeurbanne, France*
[4] *Key Laboratory of Special Function Materials and Structure Design, Ministry of Education, Lanzhou 730000, China*
(Received 25 February 2016; published 9 May 2016)

The occurrence of the bubble-like structure has been studied, in the light of pseudospin degeneracy, within the relativistic Hartree-Fock-Bogoliubov (RHFB) theory. It is concluded that the charge/neutron bubble-like structure is predicted to occur in the mirror system of $\{^{34}\mathrm{Si}, {}^{34}\mathrm{Ca}\}$ commonly by the selected Lagrangians, due to the persistence of $Z(N) = 14$ subshell gaps above which the $\pi(\nu)2s_{1/2}$ states are not occupied. However, for the popular candidate ^{46}Ar, the RHFB Lagrangian PKA1 does not support the occurrence of the bubble-like structure in the charge (proton) density profiles, due to the almost degenerate pseudospin doublet $\{\pi 2s_{1/2},\pi 1d_{3/2}\}$ and coherent pairing effects. The formation of a semibubble in heavy nuclei is less possible as a result of small pseudospin-orbit (PSO) splitting, while it tends to appear at $Z = 120$ superheavy systems which coincides with large PSO splitting of the doublet $\{\pi 3p_{3/2},\pi 2f_{5/2}\}$ and couples with significant shell effects. Pairing correlations, which can work against bubble formation, significantly affect the PSO splitting. Furthermore, we found that the influence on semibubble formation due to different types of pairing interactions is negligible. The quenching of the spin-orbit splitting in the p orbit has been also stressed, and it may be considered the hallmark for semibubble nuclei.

DOI: 10.1103/PhysRevC.93.054312

I. INTRODUCTION

Proton and neutron density distributions provide fundamental information on nuclear structure. Owing to the saturation properties of the nuclear forces, the radial dependence of the nuclear density in finite nuclei is expected to take the form of a Fermi distribution. However, the nuclear density distribution may also exhibit oscillations, namely the changing of the phase and amplitude with respect to the mass number A [1]. Therefore it is recognized in general that the density fluctuations indicate typical quantal effects related to the populating of the single-particle (s.p.) states with the wave functions which have specific spatial behavior [2]. In this context, s orbits, which are the only candidates with nonzero wave functions at the origin, play a delicate role in determining the central density profiles. Depending on whether they are populated or not, an elevation or the opposite phenomenon—depression—may emerge in the interior of the nucleus. The latter phenomenon is often referred to as the semibubble structure.

The existence of a bubble-like structure was first suggested in Ref. [3] in the 1940s, in which the nucleus was assumed to be a thin spherical shell to explain the equally spaced nuclear s.p. levels. After that, in the 1970s, extensive explanations of bubble occurrences were made by using several models, such as the liquid drop approach [4], the Thomas-Fermi model [5], as well as the Hartree-Fock method [6]. More recently, microscopic calculations using nonrelativistic and relativistic mean field models have been carried out to investigate the bubble structure for various regions of the nuclear chart, from the light [7–9], through heavy [10–12], to superheavy [13–15] regions. Novel density profiles, i.e., true bubble structures with a vanishing density at the center, were predicted in the extraordinary $Z \geqslant 240$ region [13,16]. It is also interesting to notice that the formation of the bubble-like structure is not confined to a particular region of the nuclear chart: it may be possible from light to superheavy mass regions. For the formation of the bubble-like structure it is in general required that the nucleus be spherical or just weakly deformed, and sometimes also have weak pairing correlations, to ensure a low occupation of s states.

It is also worth noticing that the nuclear tensor force [17–26], which plays a very important role in the isotopic evolution of some s.p. states, may have certain effects in determining the central density distributions. The possible existence of a proton semibubble structure in sd-shell nuclei has been reexamined within a nonrelativistic framework by taking into account the tensor force [9,11,12]. In a relativistic framework, the tensor force, however, contributes only to the Fock diagrams [27–29]. In contrast to the relativistic mean-field (RMF) approach [30–39] in which the Fock diagrams are simply dropped, the relativistic Hartree-Fock (RHF) approach [40–48] provides a relativistic platform to account for the nuclear tensor force naturally [23,27–29,48]. With the presence of the Fock terms in the mean-field channel, substantial improvements have been achieved in self-consistent descriptions of the shell structure and its evolution in the ordinary [23,48,49], exotic [29,50], and superheavy nuclei [51], and the nuclear isospin excitation modes [52–55]. Nowadays, it is rather clear that the modeling of exotic nuclei requires the development of more elaborate nuclear effective interactions that include the tensor force. Thus, the pairing correlations, tensor force, and deformation may have important implications for the semibubble formation.

On the other hand, the quasidegeneracy of two s.p. states, (n,l,j) and $(n' = n+1, l' = l-2, j' = j-1)$, indicates a

---

[*] longwh@lzu.edu.cn

hidden symmetry in nuclei, i.e., the pseudospin symmetry (PSS) [56–63]. The PSS was recognized as a property of the solutions of the Dirac equation if the sum of the Lorentz scalar and vector potentials, respectively Σ_S and Σ_0, of the system is independent of the coordinate variable $\boldsymbol{r}$, i.e., $\Sigma_S(\boldsymbol{r}) + \Sigma_0(\boldsymbol{r}) = \text{constant}$ [60,64,65]. Obviously, such a condition cannot be satisfied in a nuclear system with bound states. In realistic nuclei, the PSS is in general conserved approximately due to the delicate balance between strong attraction and repulsion represented by the scalar potential Σ_S and the vector one Σ_0, respectively. In this sense, the PSS is rather viewed as a dynamical symmetry [66,67], and it may be better conserved in exotic nuclei due to more extensive matter distributions [68]. In fact, not only the origin of PSS can be interpreted by such a covariant structure in the Dirac equation: it applies also for the strong spin-orbit (SO) effect in finite nuclei [32,34,37]. Both splittings of spin and pseudospin (PS) partners and their isospin dependence reveal interesting physics in the evolution of shell structure, particularly for exotic nuclei [63,69].

Within the RHF approach, the PSS relevant shell evolution [29,48,50,62,70] and halo formation [71,72] have been investigated, and better agreements with experimental findings have been achieved. We briefly mention here several aspects of this progress. With the inclusion of Lorentz tensor ρ-N coupling, the pseudospin-orbit (PSO) splitting induced unphysical shell closures (58 and 92) in RMF calculations [73,74] have been eliminated [48]. Also, better conservation of PSS in cerium ($Z = 58$) isotopes yields halos at the drip line [71]. The Fock terms from the isoscalar mesons are also found to play a dominant role in reproducing the $Z = 64$ subshell closure and its Z dependence [50]. Furthermore, the appearance of the $N = 184$ shell gap in superheavy nuclei [51] is associated again with a better restoration of PSS for the partners with high l. Those could clearly reveal the need for the exchange (Fock) diagrams in the relativistic scheme.

For a spherical nucleus, the $s_{1/2}$ state that plays an essential role in the bubble-like structure is in general accompanied by a $d_{3/2}$ state; they form PS partners, i.e., the pseudo-orbit $\tilde{p}$. Thus, for nuclei with PS partners $\tilde{p}$ near the Fermi surface, the relative position and occupation of the $s_{1/2}$ state are essentially related to the PSO splitting of $\tilde{p}$, as is the occurrence of the central depression in the nuclear density profile. In this work we therefore take a global survey of bubble-like structure, in the light of PSS, within the relativistic Hartree-Fock-Bogoliubov (RHFB) theory [75–77] which was established to describe weakly bound nuclei, and compare to the relativistic Hartree-Bogoliubov (RHB) calculations [36,37], as well as to the previous literature. Based on calculations with both RHFB and RHB theories, the density profiles, the bulk properties, and s.p. levels of the selected nuclei will be analyzed in detail to reveal the relevant shell and pairing effects.

The contents are organized as follows. In Sec. II, we briefly recall the general formalism of the RHFB theory and the charge-density profile. In Sec. III are detailed discussions on the emergence of bubble-like structures in the selected isotopes and isotones, including the model-reliability test. The impact of pairing correlations on bubble formation and PSO splitting is investigated in Sec. IV. The bubble-induced SO splitting is revisited in Sec. V. Finally, a brief summary is given in Sec. VI.

II. FRAMEWORK

In this work we employ the spherical RHFB approach with density-dependent meson-nucleon couplings. Details are given in Refs. [70,75,77], and we review only the main equations. The eigenvalue equation for nucleons, namely the RHFB equations in coordinate representation, have the following form:

$$\int d\boldsymbol{r}' \begin{pmatrix} h(\boldsymbol{r},\boldsymbol{r}') & \Delta(\boldsymbol{r},\boldsymbol{r}') \\ -\Delta(\boldsymbol{r},\boldsymbol{r}') & h(\boldsymbol{r},\boldsymbol{r}') \end{pmatrix} \begin{pmatrix} \psi_U(\boldsymbol{r}') \\ \psi_V(\boldsymbol{r}') \end{pmatrix} = \begin{pmatrix} \lambda + E & 0 \\ 0 & \lambda - E \end{pmatrix} \begin{pmatrix} \psi_U(\boldsymbol{r}) \\ \psi_V(\boldsymbol{r}) \end{pmatrix}, \tag{1}$$

where E is the quasiparticle energy, ψ_U and ψ_V denote the spinors of Bogoliubov quasiparticles, and the chemical potential λ is introduced to preserve the particle number on the average. The Dirac s.p. Hamiltonian h, which encloses all the long range particle-hole (ph) correlations, is of the general form

$$h(\boldsymbol{r},\boldsymbol{r}') = (\boldsymbol{\alpha}\cdot\boldsymbol{p} + \beta M) + \Sigma_H(\boldsymbol{r})\delta(\boldsymbol{r}-\boldsymbol{r}') - \Sigma_F(\boldsymbol{r},\boldsymbol{r}'). \tag{2}$$

Here the local field Σ_H contains the contributions from the Hartree and the rearrangement terms, and the nonlocal one Σ_F corresponds to the Fock terms [47,48].

The pairing field Δ, which includes the particle-particle (pp) correlations, reads as

$$\Delta_\alpha(\boldsymbol{r},\boldsymbol{r}') = -\frac{1}{2}\sum_\beta V^{pp}_{\alpha\beta}(\boldsymbol{r},\boldsymbol{r}')\kappa_\beta(\boldsymbol{r},\boldsymbol{r}'), \tag{3}$$

with κ being pairing tensor. In practice, the phenomenological pairing interactions are used in the pairing channels to obtain reasonable pairing effects, such as a finite-range Gogny force [78],

$$V(r,r') = \sum_{i=1,2} e^{-[(r-r')/\mu_i]^2}(W_i + B_i P^\sigma - H_i P^\tau - M_i P^\sigma P^\tau), \tag{4}$$

or a density-dependent δ interaction (DDDI) [79],

$$V(r,r') = V_0\frac{1}{2}(1-P^\sigma)\left(1-\frac{\rho(r)}{\rho_0}\right)\delta(r-r'). \tag{5}$$

It should be noticed that the RHFB equation (1) is a coupled integrodifferential equation and is hard to solve in coordinate space. In order to provide an appropriate description of the asymptotic behaviors of the density profile, we expand the quasiparticle spinors ψ_U and ψ_V on the Dirac Woods-Saxon (DWS) basis [80]. The basis parameters are same as in Ref. [51].

The self-consistent solutions of the RHFB equation (1) allow one to obtain all the quantities of interest, such as the density profiles, the canonical s.p. energies, etc. In this work, the charge density is determined from the proton density profile by incorporating the corrections of the center-of-mass motion and finite nucleon size. The first correction is done by using the proton density in the center-of-mass reference frame, i.e., $\rho_{\text{c.m.}}$, which is related to the Hartree-Fock (HF) point-proton density through

$$\rho_{\text{HF}}(r) = \frac{4}{B^3\pi^{\frac{1}{2}}}\int e^{-r'^2/B^2}\rho_{\text{c.m.}}(|r-r'|)dr', \qquad (6)$$

where $B^{-2} = 2\langle \boldsymbol{p}^2_{\text{c.m.}}\rangle/(3\hbar^2)$ and $\boldsymbol{p}_{\text{c.m.}}$ is the center-of-mass momentum. The second correction is taken into account by doing the convolution of $\rho_{\text{c.m.}}$ with a Gaussian representing the form factor:

$$\rho_{\text{ch}}(r) = \frac{1}{2\pi^2 r}\int_0^\infty k\sin(kr)\bar{\rho}_{\text{HF}}(k)\exp\left[\frac{1}{4}k^2(B^2-a^2)\right]dk, \qquad (7)$$

where $\bar{\rho}_{\text{HF}}(k)$ is the Fourier transform of the HF proton density and $a^2 = 2/3(0.862^2 - 0.336^2 N/Z)$ accounts for the finite nucleon size [81]. Denoting $\gamma^2 = 1/(a^2 - B^2)$, the charge-density distribution ρ_{ch} is finally derived as

$$\rho_{\text{ch}}(r) = \frac{\gamma}{\sqrt{\pi r^2}}\int r'dr'\rho_{\text{HF}}(r')[e^{-\gamma^2(r-r')^2} - e^{-\gamma^2(r+r')^2}], \qquad (8)$$

where $\rho_{\text{HF}}(r')$ corresponds to the proton density determined by the self-consistent calculations with the RH(F)B theories. For the neutron density profiles, we directly use the HF density from the RH(F)B calculations without considering the center-of-mass corrections.

III. SEMIBUBBLE CANDIDATES

The bubble-like structure is an exotic phenomenon which is characterized by distinct central depressions of the matter distributions. Bubble candidates, however, can be separated into two type: the type I semibubble occurs in *sd* shell nuclei with the *s* state depopulated, while the type II semibubble can occur in superheavy nuclei with large repulsive Coulomb field. Concerning the case of type I, either proton or neutron doublets $\tilde{p}$ nearby the Fermi surface with a large PSO splitting are possible candidates. For the case of type II, nuclei with low-l states unoccupied are favored for the bubble-like structure since high-l states are driven towards the surface of the nucleus due to the strong centrifugal potential and large Coulomb repulsion.

In the following subsections, we give a global survey of bubble-like structure going from medium mass nuclei toward superheavy ones. The calculations are performed with the RHFB and RHB theories using the optimal effective interactions available, namely the RHF ones PKA1 [48] and PKO3 [23] and the RH one DD-ME2 [82]. The Gogny D1S pairing interaction depends slightly on the mass: A general factor g is therefore introduced for its strength, as in Refs. [83,84].

A. Proton semibubble in *sd* shells

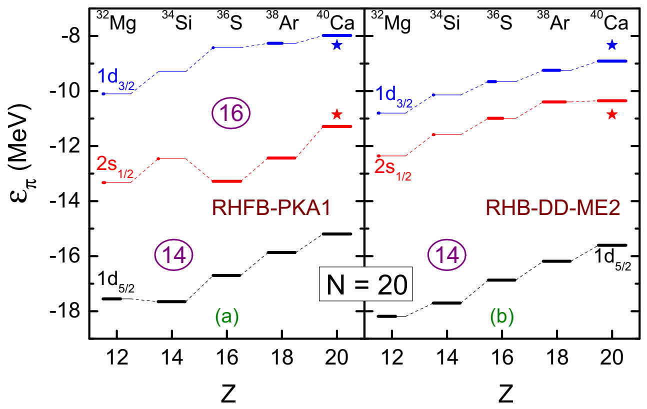

FIG. 1. Canonical proton single-particle energies along the $N = 20$ isotonic chain calculated by RHFB with PKA1 and RHB with DD-ME2. The lengths of thick bars correspond with the occupation probabilities of the proton orbits and the filled stars denote the experimental data that are taken from Ref. [85].

The nuclear charge distribution is an important observable which can provide very detailed information on nuclear structure [86,87]. For instance, the charge distribution can reflect the proton-density distribution in the nucleus, and a central depressed charge distribution is the consequence of the proton bubble-like structure. Hence, a proton-bubble nucleus can be identified experimentally from the measurement of the charge distribution, e.g., by the elastic electron-nucleus scattering experiment.

We first search for the proton semibubble in the $N = 20$ isotones. The evolutions of *sd* states and their occupations (thick bars) along the $N = 20$ isotonic chain are shown in Fig. 1 for the selected effective Lagrangians: PKA1 [plot (a)] and DD-ME2 [plot (b)]. The experimental data of the relevant s.p. energies in ^{40}Ca are also reported [85]. Among the two Lagrangians, it appears that the Lagrangian PKA1 slightly overestimates the PSO splitting between $\{\pi 2s_{1/2}, \pi 1d_{3/2}\}$ for ^{40}Ca while the DD-ME2 underestimates it. In a recent work, we have deduced that the Lorentz tensor ρ and pseudovector π meson-nucleon couplings, which can be treated as a mixture of central and tensor forces, are the important ingredients in covariant density functional (CDF) to reproduce the evolutions of the s.p. spectrum, for both *sd* and *pf* shells, in calcium isotopes [29].

For the PKA1 results presented in Fig. 1(a), the PSO splitting increases from calcium to sulfur as the valence protons are gradually removed from the orbit $\pi d_{3/2}$. When down to silicon, the $Z = 14$ subshell reaches a maximum with negligible pairing effects. Thereby, the RHF Lagrangian PKA1 predicts two subshell closures at $Z = 14$ and 16, respectively, which are consistent with the experimental trends [69,88]. Meanwhile in the DD-ME2 results [see Fig. 1(b)] we observe smooth changes, and a similar trend is also obtained by the RHF Lagrangian PKO3. Notice that the $N = 20$ closed shell structure remains for $Z \geqslant 14$ [69,89], which indicates ^{34}Si to be spherical or just weakly deformed. Moreover, both nonrelativistic and relativistic mean field approaches predict a spherical shape for ^{34}Si [84,90,91], and the $N = 20$ shell closure is robust enough to hinder significant coupling to collective states. Therefore, ^{34}Si, being almost empty in the $\pi 2s_{1/2}$ orbit, can be treated as a potential candidate of the proton semibubble.

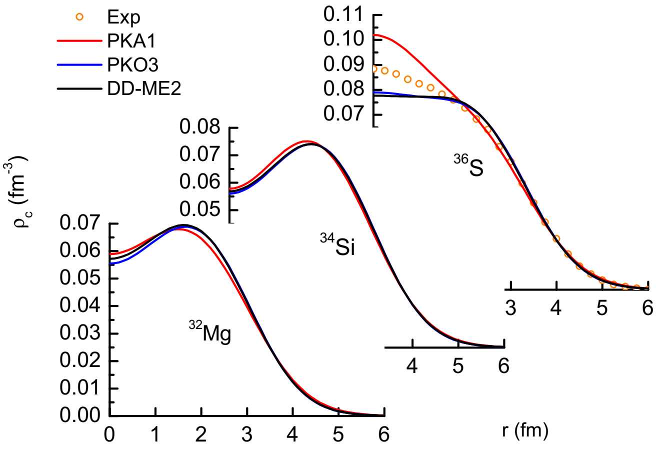

FIG. 2. Charge distributions of $N = 20$ isotones calculated by RHFB with PKA1 and PKO3 and by RHB with DD-ME2. The experimental data for ^{36}S are taken from Ref. [92].

In Fig. 2 we show the charge distributions of selected $N = 20$ isotones: ^{36}S, ^{34}Si, and ^{32}Mg. The results are calculated by RHFB with PKA1 and PKO3 and by RHB with DD-ME2. For the stable nucleus ^{36}S, the experimental charge distribution is available [92] and is reported in Fig. 2 (empty circles). The agreement with the mean-field profile is satisfactory for $r > 2$ fm. At the central region, a fully occupied $\pi 2s_{1/2}$ orbit (i.e., PKA1) leads to a bump slightly higher than the experimental data, while a partially occupied $\pi 2s_{1/2}$ orbit (i.e., PKO3 and DD-ME2) induces a lower and flat central density profile. It is worth noticing that the mean occupation probabilities of the $\pi 1d_{3/2}$ (0.08) and $\pi 2s_{1/2}$ (0.82) orbits in ^{36}S have been extracted from the ^{36}S$(d,^3$He$)^{35}$P experiment [93]. The fact that the $\pi 1d_{3/2}$ state is slightly occupied may be due to the dynamical correlations. Such correlations, which go beyond the mean field approximation, are not included in the present work. In a RH calculation—see for instance Refs. [8,94] which present results similar to PKA1—the correlations beyond mean field could improve the agreement with the data.

Since a $Z = 14$ subshell is sufficiently large ($\sim$5 MeV), the ground state of ^{34}Si is expected to be $(\pi 2s_{1/2})^{-2}$. As can be seen in Fig. 2, a more prominent proton bubble-like structure is predicted in ^{34}Si in the RH(F)B calculations for all the effective Lagrangians considered in this work. Some nonrelativistic density functionals also predict a charge-density depletion for ^{34}Si [8,9]. This possible bubble-like structure has been indirectly confirmed as an explanation of the results on the transfer reactions ^{34}Si$(d,p)^{35}$Si and ^{36}S$(d,p)^{37}$S. It is found that the splitting between the major fragments of neutron $3/2^+$ and $1/2^+$ levels in the $2p$ shell is decreased from ^{37}S ($\sim$1.7 MeV) to ^{35}Si ($\sim$1.1 MeV) [95]. We shall discuss this aspect latter. As shown in Ref. [94], the correlations beyond the relativistic mean field give an opposite but small effect in the formation of proton bubble-like structure of ^{34}Si. Therefore, there still remains the possibility that the semibubble survives in ^{34}Si. Future experiments on the charge density of this nucleus are much awaited.

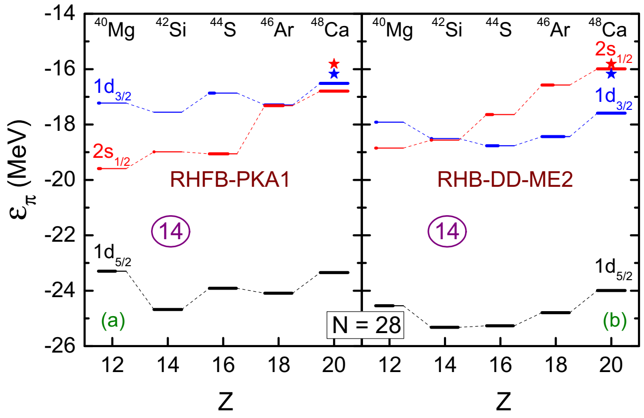

FIG. 3. Same as Fig. 1, but for $N = 28$ isotones.

We now turn to the $N = 28$ isotones. Similarly to the case of $N = 20$ isotones, we first refer to Fig. 3 where the s.p. energies and their occupations are shown. It is seen that PKA1 predicts an almost perfect degeneracy between the PS doublet $\{\pi 2s_{1/2},\pi 1d_{3/2}\}$ in ^{48}Ca and ^{46}Ar, and gives a deeper bound $\pi 2s_{1/2}$ state than $\pi 1d_{3/2}$ for the isotones with $Z < 18$. As $\pi 2s_{1/2}$ is the dominant valence configuration, the formation of the proton bubble-like structure is therefore blocked in the isotones from ^{44}S to ^{46}Ar; see Fig. 4. It has to be mentioned that most of the effective interactions investigated so far, even including phenomenological or realistic tensor force, have failed to reproduce the absolute values of PSO splitting in ^{48}Ca [9,11]. In addition, the spin-parity J^π of ^{45}Cl deduced from the neighboring nuclides is $3/2^+$ [96], confirming the order of the PS partners $\tilde{p}$ in ^{44}S predicted by PKA1.

Different from PKA1, the calculations with DD-ME2 (which does not contain the Fock terms or Lorentz tensor ρ coupling) present a large PSO splitting in ^{48}Ca and ^{46}Ar ($\sim$1.5 MeV), and an inversion of the order of the PS doublet for $Z < 14$. Since the valence protons are filled mainly in

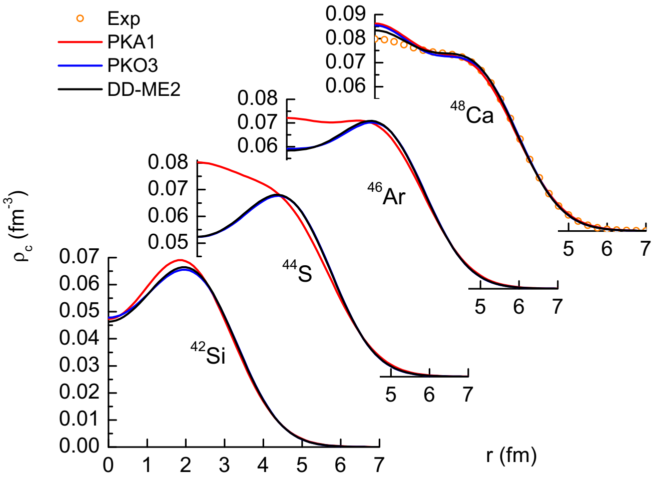

FIG. 4. Charge distributions of $N = 28$ isotones calculated by RHFB with PKA1 and PKO3 and by RHB with DD-ME2. The experimental data for ^{48}Ca are taken from Ref. [97].

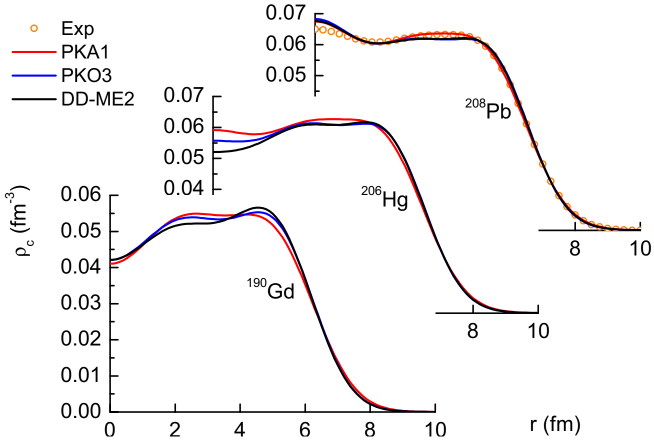

FIG. 5. Charge distributions of $N = 126$ isotones, calculated by RHFB with PKA1 and PKO3 and by RHB with DD-ME2. The experimental data for ^{208}Pb are taken from Ref. [97].

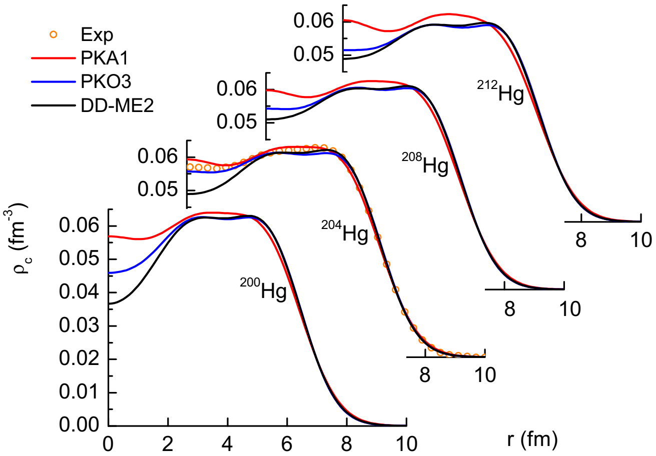

FIG. 6. Charge distributions of Hg isotopes, calculated by RHFB with PKA1 and PKO3 and by RHB with DD-ME2. The experimental data for ^{204}Hg are taken from Ref. [101].

$\pi 1d_{3/2}$, it leads to central depressions in the charge-density profiles from ^{44}S to ^{46}Ar; see Fig. 4. Similar systematics are also found in the proton spectra determined by PKO3. Here, we would like to stress that the occurrence of the bubble-like structures is tightly related not only to the order of the PS doublet $\{\pi 2s_{1/2}, \pi 1d_{3/2}\}$ but also to their splittings. As shown in Fig. 3(b), although the order of $\pi 2s_{1/2}$ and $\pi 1d_{3/2}$ is reversed at $Z = 14$, the emergence of the proton bubble-like structure in ^{44}S and ^{46}Ar is still not favored very much by DD-ME2 (see Fig. 4) because of the fairly large occupations ($v^2 > 0.2$) in $\pi 2s_{1/2}$ induced by the pairing effects, which is essentially influenced by the energy gap between the states. The RH calculation with nonlinear interactions also predicted similar density profiles as the one given by DD-ME2 [98]. For the popular candidate ^{46}Ar, shell model calculations using *sdpf* interaction [99] also predict around 0.6 occupation probability for the $\pi 2s_{1/2}$ state.

Finally, the central depressions only exist in the charge-density profiles of ^{42}Si and ^{40}Mg in $N = 28$ isotones as a consequence of the persistence of the $Z = 14$ subshell. However, the $N = 28$ shell closure is progressively eroded below the doubly magic ^{48}Ca nucleus [100]. The inclusion of the deformation and dynamical corrections would wash out the central depressions. Therefore, the emergence of a proton semibubble structure in the $N = 28$ isotones is not much favored.

We turn now to the next proton *sd* shell nuclei, i.e., the mercury ($Z = 80$) isotopes. All the measured J^π of even-N thallium ($Z = 81$) isotopes are $1/2^+$ in the ground state [96], showing a normal level sequence of the PS doublet, i.e., $\epsilon_{\pi 3s_{1/2}} > \epsilon_{\pi 2d_{3/2}}$. This is also true in our calculations, leading to a certain central depression in the proton density profiles of the mercury isotopes. We show in Fig. 5 the charge distributions of ^{208}Pb and ^{206}Hg, calculated by RHFB with PKA1 and PKO3 and by RHB with DD-ME2. The experimental data of PSO splitting for ^{208}Pb is available [85]: 0.36 MeV. In our theoretical calculations it is determined to be 0.68, 1.15, and 1.02 MeV, respectively by PKA1, PKO3, and DD-ME2. Such deviations among the Lagrangians will affect the charge density profiles for ^{206}Hg and its neighboring isotopes. The depletion of the central density in ^{206}Hg, as compared to ^{208}Pb, is quite visible for DD-ME2, while it is less pronounced for PKO3 and much less for PKA1. Since the central charge density in ^{208}Pb is somewhat enhanced, the depletion in ^{206}Hg does not lead to the development of a significant central depression.

Since a central depression in ^{206}Hg is not active, it is thus interesting to check the formation of a semibubble in its neighboring isotopes. Figure 6 displays the isotopic evolution of the charge density from ^{200}Hg to ^{212}Hg using the RH(F)B approach with the selected effective Lagrangians. The experimental data of ^{204}Hg taken from Ref. [101] are also shown for comparison. Notice that these nuclei are predicted to have spherical ground states by various deformed mean field models [84,90,91]. The calculated charge density distribution, especially the interior region, exhibits visible deviations between the selected effective Lagrangians. These deviations can be preliminarily interpreted by the evolution of shell structure in Fig. 7 where the valence proton s.p. energies and their occupation probabilities are presented. From Fig. 7 one can find that much stronger shell effects between $\pi 3s_{1/2}$ and the state just in below are provided by DD-ME2 than by PKA1. In the PKA1 results, the PSO splitting between $\pi 3s_{1/2}$ and $\pi 2d_{3/2}$ in $^{200\text{–}212}$Hg is found to be around 1.0 MeV and reaches a minimum in ^{206}Hg, and the intruder state $\pi 1h_{11/2}$ is located between, giving rise to sizable pairing excitation in these nuclei. In contrast, in the DD-ME2 results, the PSO splittings are significantly larger than the ones predicted by PKA1, and the intruder state $\pi 1h_{11/2}$ is located below the $\pi 2d_{3/2}$ state, suppressing much the pairing excitation. As a consequence, the smaller PSO splitting given by PKA1 is therefore associated with a flatter central density in $^{200\text{–}212}$Hg. The depletion in the center of the charge (proton) density of the mercury isotopes is, however, less pronounced than in silicon isotopes. We have also noticed that, in the nonrelativistic Skyrme-Hartree-Fock calculation, the tensor force could modify the order of the valence orbits $\pi 3s_{1/2}$, $\pi 2d_{3/2}$, and $\pi 1h_{11/2}$ in ^{206}Hg [12], and in PKA1 the tensor

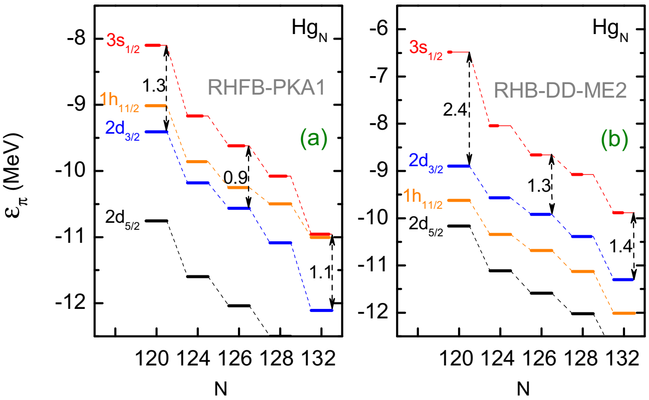

FIG. 7. Canonical proton single-particle energies along the Hg isotopic chain calculated by RHFB with PKA1 and by RHB with DD-ME2. The lengths of thick bars correspond to the occupation probabilities of the proton orbits. The size of pseudospin-orbit splitting is indicated with the value in units of MeV.

force components have been introduced naturally with the Fock diagrams [27,28].

Starting from ^{208}Pb, along the $N = 126$ isotonic chain down to the neutron drip line, the valence protons are gradually removed from the $\pi 3s_{1/2}$ state. One thus expects that more pronounced central depression may appear in the $Z = 50$–64 region. We choose the ^{190}Gd ($Z = 64$) nucleus shown in Fig. 5 to illustrate such a general feature. The depletion of the central density in ^{190}Gd relative to ^{208}Pb and ^{206}Hg is very visible. We have also checked that the central depression in the proton density profiles occurs in the $Z = 40$–64 region (for instance, in ^{122}Zr, ^{132}Sn, and ^{146}Gd) along the $N = 82$ isotonic line as well as in the $Z = 40$–50 region (for instance, in ^{90}Zr) along the $N = 50$ isotonic line. Some charge density distributions in this region obtained with a RH model can be found in Refs. [102,103], in which the authors focus on electron scattering.

B. Neutron semibubble in *sd* shells

Unlike charge densities, which can be measured precisely from the elastic scattering of electrons, there exist large uncertainties in neutron density profiles. With the development of experimental technology, the neutron densities of more nuclei are expected to be measured. For instance, parity-violating electron scattering has been suggested to measure neutron densities [104,105]. Following the exploration in previous subsection, we search for a neutron semibubble, focusing on the $N = 14$, 18, and 80 regions.

First, a neutron semibubble may occur in the neutron-rich oxygen isotopes, where ^{22}O and ^{24}O behave as doubly magic nuclei due to the large $N = 14$ and 16 subshell gaps [106–111], respectively. This leads to ^{22}O as a good candidate for a neutron semibubble nucleus. Figure 8 displays the neutron density profiles of ^{22,24}O calculated self-consistently by the RH(F)B models with the selected Lagrangians. The central neutron density in ^{24}O is somehow enhanced for PKA1 since the magicity of $Z = 16$ in this nucleus can be only confirmed by PKA1 [29]. Unfortunately, all the selected effective Lagrangians do not give a robust $N = 14$ subshell in ^{22}O, leading to fairly flat central density profiles. As a conceptual test the neutron density with the pairing channel switched off is also shown in Fig. 8 (see the dash-dotted line), and the central hole in ^{22}O becomes clearly visible. If a spherical character for ^{22}O is confirmed, it could form a bubble configuration. Measurements of the β_2 value of ^{22}O are therefore eagerly awaited.

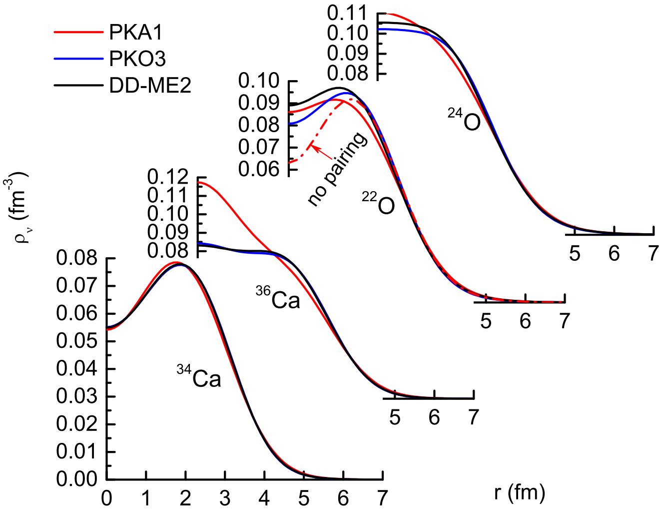

FIG. 8. Neutron distributions of $N = 14$ isotones ^{22}O, ^{34}Ca and $N = 16$ isotones ^{24}O, ^{36}Ca, calculated by RHFB with PKA1 and PKO3 and by RHB with DD-ME2.

Moving upward on the proton-rich side, the drip-line nucleus ^{34}Ca could be another candidate for a neutron semibubble nucleus although, it has not been observed so far. In Fig. 8 we also present the neutron density distributions of ^{34,36}Ca. The central neutron density of ^{36}Ca is strongly enhanced for PKA1 since an $N = 16$ subshell closure holds well on the proton-rich side. Experimentally, the break in single-neutron separation energy S_n favors a possible $N = 16$ shell gap in proton-rich calcium isotopes [112]. Meanwhile, in the calculations with PKO3 and DD-ME2 the shell effects are depressed much, and the enhanced pairing effects lead to a flat central density. By removing two neutrons from ^{36}Ca, it yields a strong depletion in the interior neutron density of ^{34}Ca; see Fig. 8. In this case, the RH(F)B results show a mild model dependence, just as in its mirror system ^{34}Si.

For the $N = 18$ isotones, the measured J^π values of the ground states of the $N = 19$ isotones are $3/2^+$, with the exception of ^{31}Mg [96], showing signal for a weak *sd* inversion. In our calculations the sequence of PS doublet is $\epsilon_{\nu 1d_{3/2}} > \epsilon_{\nu 2s_{1/2}}$ along the whole $N = 18$ isotonic chain. Therefore, the appearance of a neutron semibubble in medium mass nuclei is associated with the persistence of the $N = 16$ subshell, which has been discussed above.

We now turn to the $N = 80$ isotonic chain where most of the isotones are predicted to be of spherical shape, except those close to drip line [84,90,91]. Taking ^{120}Zr, ^{130}Sn, and ^{144}Gd as examples, it is found that the absolute values of the PSO splitting between $\{\nu 3s_{1/2}, \nu 2d_{3/2}\}$ are less than 1.0 MeV, although an inversion emerges around $Z = 50$. Therefore, just as in the $Z = 80$ case, a neutron bubble-like structure in the relevant isotones is not much favored, either.

C. Semibubble in superheavy nuclei

Superheavy nuclei (SHN) are stabilized by quantum shell effects, i.e., by a considerably reduced level density around the Fermi surface which forms a shell gap. Theoretically, the studies of superheavy structure in different approaches show that the magic shells beyond the doubly magic nuclei ^{208}Pb are very model dependent. For a long time the island of stability has been predicted by the CDF models to be in the region around $Z = 120$ [51,113–115]. Furthermore, bubble configurations were also predicted in superheavy and hyperheavy nuclei with $Z \geqslant 120$ [13,116]. This phenomenon is due to the fact that, for those very-large-Z systems, a hollow charge distribution is energetically favored to lower the Coulomb repulsion.

The proton s.p. spectra of $Z = 120$ isotopes obtained in spherical RH(F)B calculations are plotted in Fig. 9. Here we take nuclei with $N = 172$, 184, and 198 as representative cases for a detailed investigation of the shell structure. It has been argued in Ref. [51] that the proton shell closure $Z = 120$ coincides with a large PSO splitting. In the present work, we discuss the link between the size of the shell gap and the density profile. We display in Fig. 10 the proton (neutron) density of the selected nuclei. It is shown that the $Z = 120$ isotopes have depressed interior proton densities. However, the minimal value does not appear at $r = 0$ since in nuclei with $Z \geqslant 82$ the $\pi 3s_{1/2}$ state that contributes to the density at $r = 0$ is fully occupied. From ^{208}Pb to larger Z systems, the nucleons will gradually occupy the high-l orbits, leading to the central-depressed neutron and proton density profiles in the superheavy systems. As seen from Fig. 10, the proton and neutron density profiles show spontaneous evolution behavior with the neutron number changing from 172 to 198.

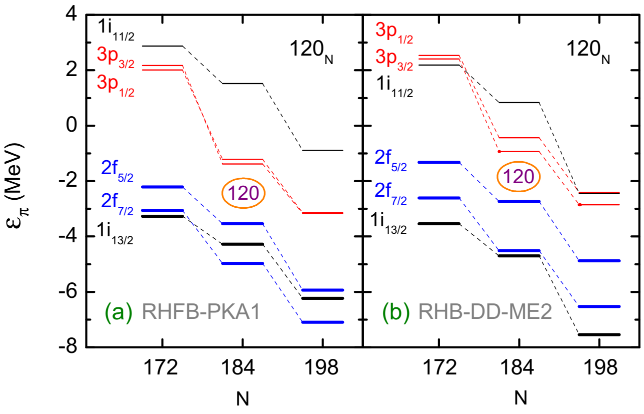

FIG. 9. Proton single-particle states at spherical shape in the nuclei ^{292}120, ^{304}120, and ^{318}120, calculated by RHFB with PKA1 and RHB with DD-ME2. The lengths of thick bars correspond to the occupation probabilities of the orbits.

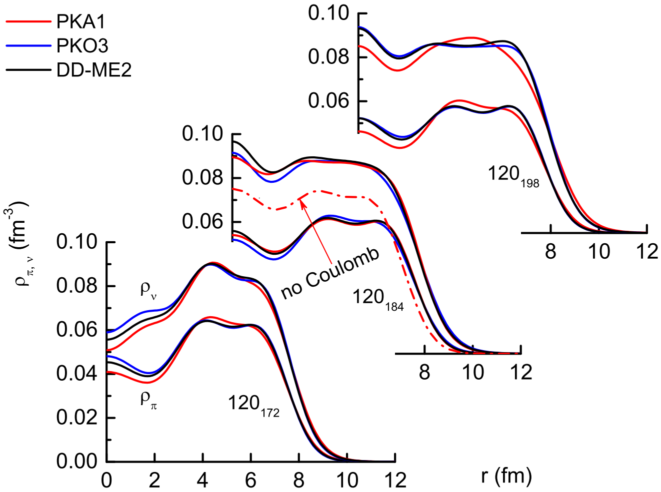

FIG. 10. Neutron and proton distributions of $Z = 120$ isotopes calculated by RHFB with PKA1 and PKO3 and by RHB with DD-ME2.

To illustrate the effect of Coulomb repulsion, self-consistent calculations have been performed with the Coulomb field switched off and the obtained proton density of ^{304}120 (in dash-dotted line) calculated by PKA1 is also shown in Fig. 10 for comparison. It is clearly seen that, for large-Z systems, the proton density profile, mainly the interior region, is changed much by the considerable Coulomb repulsion, and the protons lying in high-l orbits could be more sensitive to that. We also found that the $Z = 120$ shell closure collapses with the Coulomb field switched off and this leads to a 50% occupation probability for the $\pi 3p$ states above the shell. Therefore, the enhanced Coulomb field in large-Z systems plays a significant role in depressing the interior region of the matter distributions, as well as in giving the magic shell $Z = 120$.

As a consequence of central-depressed matter distributions, the SO splitting is reduced remarkably for the low-l states $\pi 3p$ which have more overlap with the interior depression, and it is reduced less for high-l orbits, for instance the nearby $\pi 2f$ states. Consistently the splitting between neighboring PS partners $\{\pi 3p_{3/2}, \pi 2f_{5/2}\}$ is somewhat enlarged, which thus corresponds to the emergence of a proton magic shell $Z = 120$. The semibubble deduced doubly magic nucleus ^{292}120 has been extensively discussed [15,117], although it is very close to being unbound (see Fig. 9). As shown in Fig. 10, the valence neutrons show a distinct polarizing effect on the $Z = 120$ core. From $N = 172$ to 184 the valence neutrons start to fill the low-l states $\nu 4s$ and $\nu 3d$, which leads to fairly flat neutron density profiles in the interior region for $N = 184$ isotopes [14]. Due to the proton-neutron correlations, the proton density profile for the nuclide ^{304}120 is affected consistently and becomes less depressed in the interior region. As a result, the shell gap $Z = 120$ is somewhat reduced at $N = 184$; see Fig. 9. Up to $N = 198$, the valence neutrons gradually occupy the high-l neutron orbits ($1j_{13/2}$ and $2h_{11/2}$), the density distribution given by PKA1 becomes less flat in the $N = 198$ system, and thus the $Z = 120$ shell gap is enlarged [see Fig. 9(a)].

D. Remarks

Let us finish this section with some general remarks. Combining the results presented above, it can be concluded that the charge/neutron bubble-like structure is predicted to occur commonly in the mirror system of $\{^{34}\mathrm{Si}, ^{34}\mathrm{Ca}\}$ by the selected RHF and RH Lagrangians, due to the persistence of $Z(N) = 14$ subshell gaps where the $\pi(\nu)2s_{1/2}$ states are not occupied. However, for the popular candidate ^{46}Ar, the RHF model PKA1 does not support the occurrence of the bubble-like structure in the charge (proton) density profiles, due to a near degeneracy between the PS doublet $\{\pi 2s_{1/2},\pi 1d_{3/2}\}$ in ^{46}Ar and ^{48}Ca.

Concerning heavy *sd* systems, both charge and neutron bubble-like structures are less possible as a consequence of small PSO splitting, where the pairing correlations play a decisive role and therefore the densities get contributions from both PS partners and the nearby orbits. In contrast, a more pronounced central depression may appear at $N(Z) = 40$–64 regions where the $\pi(\nu)3s_{1/2}$ states are depopulated.

Semibubble nuclei were also predicted for the $Z \sim 120$ nuclei located around the center of the predicted island of stability of SHN. Below the shell $Z = 120$, the protons filling the high-l states will be driven toward the surface of the nucleus due to the strong centrifugal potential and large repulsive Coulomb field. Both effects lead to an interior depression of the proton distributions. The typical example is the consistent relation between density distributions and the size of $Z = 120$ shell gap.

As a short summary, we plot the contours of the neutron and proton densities in Fig. 11 for the semibubble candidates ^{34}Si, ^{34}Ca, ^{190}Gd, and ^{292}120. For light systems, namely the mirror nuclei ^{34}Si and ^{34}Ca, distinct central depressions can be observed in the proton and neutron density profiles, respectively. For a heavy system, like ^{190}Gd, the neutron density profile shows a relatively weak central depression with rather narrow range. Extending to the superheavy system ^{292}120, the semibubble structure becomes evident again, not only for the neutron density profile but also for the proton one.

IV. PAIRING EFFECTS

It is widely recognized that pairing correlations may hinder bubble formation since the scattering of Cooper pairs could populate the *s* state, raising the central area of the density profile of the nucleus. In this section, we shall study the effect of pairing on semibubble formation, as well as the interplay between shell effects and pairing correlations.

A. Pairing: Surface or volume?

The study of the pairing effect in a semibubble candidate is rather delicate since it occurs in a two-hole state from a (sub)shell closure near the *sd* orbits. Although, as stressed above, there are strong indications that the $\pi 2s_{1/2}$ is largely populated in ^{46}Ar, we choose this nucleus as a representative to illustrate the impact of pairing correlations on the semibubble occurrence. For ^{46}Ar, the pairing effects are mainly involved by the PS partners $\{\pi 2s_{1/2},\pi 1d_{3/2}\}$, among which the wave function of $\pi 1d_{3/2}$ state is localized in the surface region whereas the one of $\pi 2s_{1/2}$ distributes at small distances. It is therefore worth checkin whether the density profile will be modified by the nature of the pairing force.

We utilize two Lagrangians, PKA1 and DD-ME2, as the representatives, which predict quite different charge density profiles for ^{46}Ar, and compare the calculations with two kinds of pairing interactions: the surface DDDI and the volume one without the density-dependent term $\rho(r)/\rho_0$ in Eq. (5), abbreviated as DI (δ interaction). For both surface and volume pairing forces, the pairing strength V_0 in Eq. (5) is fitted to match the pairing gap obtained with the finite-range pairing force D1S, and we considered in this study a simple cutoff scheme, which was set to be 100 MeV in quasiparticle space.

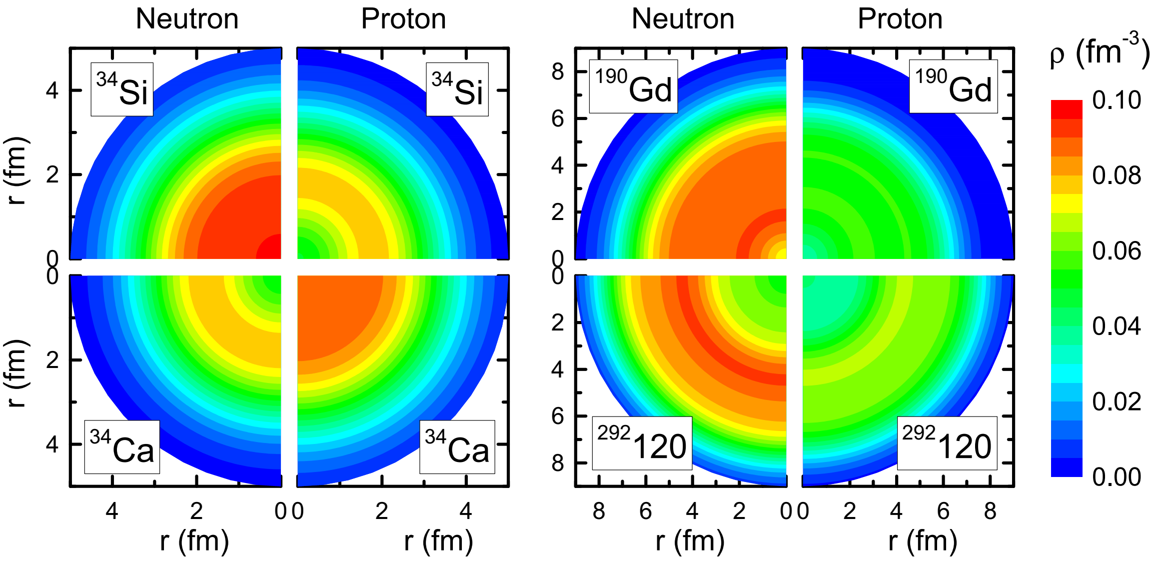

FIG. 11. The contour of neutron and proton densities for the semibubble candidates ^{34}Si, ^{34}Ca, ^{190}Gd, and ^{292}120, calculated by RHFB with PKA1.

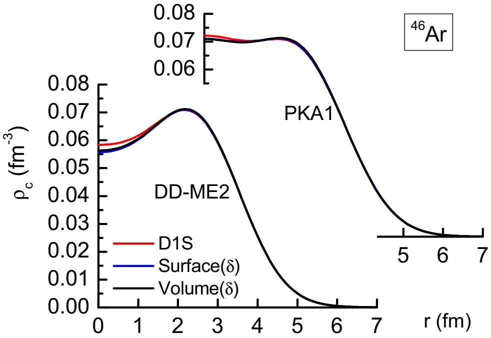

FIG. 12. Charge distributions of ^{46}Ar calculated by RH(F)B with different pairing interactions.

The obtained charge density profiles with different kinds of pairing interactions are shown in Fig. 12. It is observed that the calculations with the surface- and volume-type δ pairing forces give almost identical charge distributions. In contrast, the calculations with the Gogny D1S pairing interaction present slightly enhanced central density profiles for both PKA1 and DD-ME2, which is due to the effect of the finite-range nature of the interaction [118], the $\pi 2s_{1/2}$ orbit being more populated. In fact, if we slightly increase the strength of the δ pairing force, it can reproduce almost exactly the results of the D1S case. In Ref. [119] it was also stressed that the radial distribution of pairing correlations in finite nuclei is not strongly correlated to the surface or volume character of the pairing force but rather to the localization of the s.p. states close to the Fermi surface.

B. Pseudospin-orbit splitting

To further illustrate the impact of pairing correlations on the PSO splitting as well as the semibubble formation, we vary the pairing interaction strength arbitrarily and correlate the PSO splittings with the proton pairing gaps Δ. Figure 13 shows the results calculated with the pairing interactions D1S [plot (a)] and DDDI [plot (b)] using the PKA1 Lagrangian, where the average pairing gap Δ goes from 200 keV to the realistic value 1.80 MeV by varying the strengthes of the pairing forces.

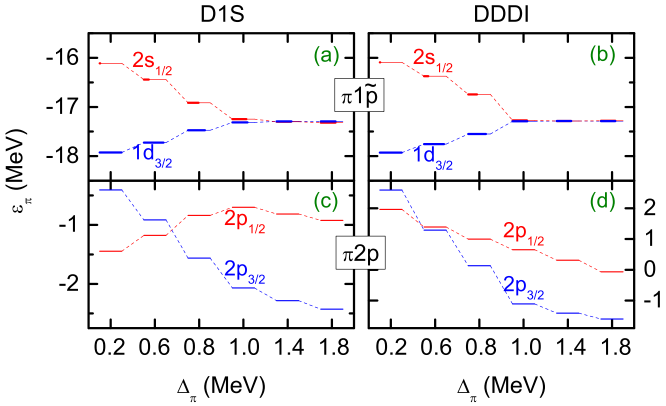

FIG. 13. The $\pi 1\tilde{p}$ PSO and $\pi 2p$ SO splittings in ^{46}Ar as a function of the neutron pairing gap, calculated from PKA1 with Gogny D1S (a,c) and DDDI (b,d) pairing forces. The lengths of thick bars correspond to the occupation probabilities of the orbits.

Comparing Figs. 13(a) and 13(b), there is no distinct difference of the s.p. energies and occupation probabilities between the finite-range D1S force and zero-range DDDI at various pairing gaps. Notice that, due to the existence of fairly large shell gaps 14 and 20 respectively below and above the PS partners $\tilde{p}$ [see Fig. 3(a)], the scattering of Cooper pairs can only happen between the PS partners. It is found that, with weak pairing correlations, the splitting of the PS partners can be as large as ∼1.8 MeV, and the $\pi 2s_{1/2}$ state is not much populated. It therefore provides the chance of a bubble formation in ^{46}Ar. As the pairing correlations were enhanced, the splitting decreases gradually. For PKA1, the PSO splitting reaches a degeneracy at $\Delta = 0.80$ MeV and holds it until $\Delta = 1.80$ MeV, leading to the flat central density profile as shown in Fig. 4. For DD-ME2, there is still a large shell gap ∼2.0 MeV at $\Delta \approx 1.80$ MeV and the $\pi 2s_{1/2}$ orbit is slightly occupied, leading to a weak dip at the central part of charge density; see Figs. 3 and 4. It is interesting to notice that the energy centroid of the PS partners $\tilde{p}$ is fairly independent of the pairing strength.

We display also in Figs. 13(c) and 13(d) the canonical s.p. energies of $\pi 2p$ states. For those weakly bound or unbound states, the s.p. energies given by the calculations with finite-range D1S pairing force and zero-range DDDI are different while still identical on the trend. The energies of unbound states have been checked by changing the box size, and they weakly depend on the radial cutoff. Coincident with the relation between the SO effects and PSS conservation pointed out in Ref. [120], the substantial SO effects, i.e., at $\Delta = 1.0$–1.8 MeV, lead to reduced splitting between PS partners, whereas the quenched or inverted SO effects, i.e., at $\Delta = 0.2$–0.8 MeV, correspond to remarkable violation of PSS.

As a consequence, the emergence of the bubble-like structure is not only tightly related to the s.p. configurations near the Fermi surface, namely the position of the orbits $\pi 2s$ and $\pi 1d$ and the gaps between, but also to the effects of the pairing correlations, especially its strength. It is now rather clear that the modeling of bubble-like nuclei also requires the proper treatment of the pairing correlations in the pp channel.

V. BUBBLE-INDUCED SPIN-ORBIT SPLITTING

In mean-field approaches, the SO interaction scales with the derivative of the nucleon densities (or mean potentials). It is thus believed to be peaked at the surface where this derivative may reach the maximum. Notice that, in the RHFB model, the Fock terms contribute complicated corrections [62,121]. A central depletion of the proton (neutron) density could induce a valuable derivative of the densities (or mean potentials) at the central region and thus reduce the strength of the SO interaction. Since the derivative of the depressed density (or mean potential) in the interior of the nucleus is of the opposite sign to the one obtained at the surface, it yields a global reduction of the SO interaction for nucleons located in the center. As the strong centrifugal barrier may prevent nucleons with high-l from residing there, such a reduction of the SO

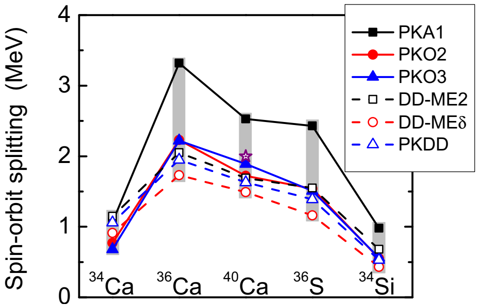

FIG. 14. The SO splittings of $\nu 2p$, calculated by different Lagrangians. The experimental value (star) of ^{40}Ca [85] is also displayed as a reference.

TABLE I. The relative changes of $\nu 2p$ SO splitting in %, calculated by different RHF and RH Lagrangians. The data inside the parentheses denote the contributions from rank-2 tensor components of Fock diagrams. See the text for details.

Force	$^{34\leftarrow 36}$Ca	$^{36\leftarrow 40}$Ca	^{40}Ca → ^{36}S	^{36}S → ^{34}Si
PKA1	−68% (3%)	31% (−18%)	− 5% (−6%)	−60% (4%)
PKO2	−65% (2%)	23% (−17%)	−13%(2%)	−64% (2%)
PKO3	−69% (2%)	18% (−23%)	−19% (−8%)	−63% (6%)
DD-ME2	−44%	21%	−9%	−56%
DD-MEδ	−47%	16%	−22%	−63%
PKDD	−46%	20%	−15%	−62%

interactions may have more distinct effects on the low-l orbits, i.e., mainly for p states.

The quenching of the SO splitting in p orbits has been advertised as the hallmark for semibubbles in ^{46}Ar and ^{206}Hg [10]. However, the possibility of a bubble structure in these nuclei has been ruled out by our theoretical calculations as well as by experimental information [99,101]. Here, we intend to discuss the reductions of $\nu 2p$ SO splittings in ^{34}Si and ^{34}Ca. We start from doubly magic ^{40}Ca, proceed to the s-filled nuclei ^{36}S (^{36}Ca), and reach the semibubble candidates ^{34}Si (^{34}Ca), using selected RHF Lagrangians PKA1 [48], PKO2, and PKO3 [23], as well as RH ones DD-ME2 [82], DD-MEδ [122], and PKDD [123]. Through this extensive analysis, we expect to get some general conclusions which would be less dependent on CDF modelings.

For simplicity, we perform HF calculations by neglecting pairing correlations. All the calculated SO splittings of the neutron $\nu 2p$ orbit are reported in Fig. 14. The experimental value extracted from the centroids of $\nu 2p$ is available only for the nucleus ^{40}Ca, which is ~2.0 MeV [85]. It is clearly seen that the PKA1 calculation overestimates the $\nu 2p$ splitting while the others underestimate it with respect to the experimental value. Notice that the $\nu 2p$ levels are far above the Fermi surface; the dynamical coupling to the core vibrations, which is not considered in current calculations, might be one missing physical mechanism to diminish the existing disagreement.

A general trend can be observed in Fig. 14. From ^{40}Ca down to the neutron-rich nucleus ^{36}S, the SO splitting decreases by removing four protons in the $\pi d_{3/2}$ level, whereas up to the proton-rich nucleus ^{36}Ca the SO splitting increases by removing four neutrons in the $\nu d_{3/2}$ level. As expected, in all cases both splittings decrease from bump-like nucleus ^{36}S (^{36}Ca) to bubble-like nucleus ^{34}Si (^{34}Ca). Our calculations are qualitatively consistent with the recently observed reduction of the $\nu 2p$ SO splitting from ^{37}S to ^{35}Si, by using the major fragments to evaluate the SO splittings [95].

To better visit the evolution of $\nu 2p$ splitting, we summarize all the relative changes in Table I. From bump-like nucleus to bubble-like one, one expects that the reduction of $2p$ SO splitting is mainly produced by pure SO effects. We have found in all cases a reduction of about 60% from ^{36}S down to ^{34}Si. However, the reduction from ^{36}Ca to ^{34}Ca seems to strongly depend on the models: ~67% for the RHF models and ~45% for the RH ones.

On the other hand, from ^{40}Ca to the bump-like nucleus ^{36}S (^{36}Ca), the situation is quite complex. One has to recognize that the effects of the symmetry energy, SO coupling, and tensor force are delicately connected with the modeling of the s.p. spaces along isotopic and isotonic lines. From ^{40}Ca to ^{36}S, PKO2 shows a reduction of ~13%, while it is more pronounced for PKO3 that contains the isovector π coupling. It seems that the deviations between PKO2 and PKO3 are mainly due to the effects of the tensor force brought about by the π meson. For PKA1, which contains both π-pseudovector and ρ-tensor couplings, the situation is quite different, with a rather small reduction dominated by the tensor force. It may be due to the fact that PKA1 provides a different balance of nuclear attraction and repulsion compared to the RHF model's PKO series and the RMF ones, caused by the fairly strong tensor ρ field [48]. Moving to other direction, from ^{40}Ca to ^{36}Ca, all the selected models present the opposite trend to the case from ^{40}Ca to ^{36}S, and the SO splittings of the $\nu 2p$ orbit are distinctly enhanced. It is also interesting to notice that, opposite to the whole trend, the tensor force components brought about by the Fock diagrams present a sizable reduction of the SO splitting (see the RHF results in Table I), and the tensor effects are dominated by the isoscalar Fock diagrams, namely the exchange terms of σ-scalar and ω-vector couplings [27].

In conclusion of this section, we illustrate again that the quenching of the low-l p splitting is a general feature in semibubbles and it may be considered the hallmark for semibubble candidates due to the fact that similar systematics is also found in the nonrelativistic calculations by taking into account the tensor force [124].

VI. SUMMARY

This work was undertaken to give a global survey of bubble-like structure of exotic nuclei using the RHFB theory. The occurrences of charge and neutron bubbles respectively in ^{34}Si and ^{34}Ca are predicted, mainly due to the fact that the orbits $\pi(\nu)2s_{1/2}$ are not occupied by the valence particles. In ^{46}Ar, the inversion of the proton orbits $\pi 2s_{1/2}$ and $\pi 1d_{3/2}$ is not supported by the RHF Lagrangian PKA1 that presents nearly degenerate PS partners (i.e., $\pi 1\tilde{p}$) for both ^{46}Ar and ^{48}Ca. It thus hinders the occurrence of the proton bubble-like structure in argon isotopes. The formation of semibubbles in heavy nuclei is not much favored, at least by the selected models. For superheavy systems, fairly strong shell effects are found to favor the formation of semibubbles. For instance, semibubbles are predicted for the semimagic $Z = 120$ systems and the ones nearby, in which the coupling between density distribution and magicity is found to be significant. In addition it has been noticed that another antibubble effect, namely the dynamical correlation, would quench the bubble structure in the ground state of semibubble candidates to a certain extent.

We have also analyzed the influence of the type of pairing interaction on the semibubble formation. The calculations with finite-range pairing force Gogny D1S and zero-range δ forces (both the surface and volume ones) give nearly identical density profiles and single-particle configurations. In particular, it is found that the pairing correlations may significantly decrease the PSO splitting, leading to well preserved PSS if the pairing gap is comparable with the PSO splitting given by the HF calculations. Finally, the quenching of the SO splitting in the neutron p orbit has been stressed, and it could be considered the hallmark for semibubble candidates.

ACKNOWLEDGMENTS

This work is partly supported by the National Natural Science Foundation of China under Grant No. 11375076, and the Specialized Research Fund for the Doctoral Program of Higher Education under Grant No. 20130211110005.

---

[1] J. Friedrich and N. Voegler, Nucl. Phys. A **373**, 192 (1982).
[2] M. Brack, J. Damgaard, A. S. Jensen, H. C. Pauli, V. M. Strutinsky *et al.*, Rev. Mod. Phys. **44**, 320 (1972).
[3] H. A. Wilson, Phys. Rev. **69**, 538 (1946).
[4] W. J. Swiatecki, Phys. Scr. **28**, 349 (1983).
[5] G. Saunier, B. Rouben, and J. Pearson, Phys. Lett. B **48**, 293 (1974).
[6] X. Campi and D. W. L. Sprung, Phys. Lett. B **46**, 291 (1973).
[7] E. Khan, M. Grasso, J. Margueron, and N. Van Giai, Nucl. Phys. A **800**, 37 (2008).
[8] M. Grasso, L. Gaudefroy, E. Khan, T. Nikšić, J. Piekarewicz *et al.*, Phys. Rev. C **79**, 034318 (2009).
[9] H. Nakada, K. Sugiura, and J. Margueron, Phys. Rev. C **87**, 067305 (2013).
[10] B. G. Todd-Rutel, J. Piekarewicz, and P. D. Cottle, Phys. Rev. C **69**, 021301(R) (2004).
[11] Y. Z. Wang, J. Z. Gu, X. Z. Zhang, and J. M. Dong, Phys. Rev. C **84**, 044333 (2011).
[12] Y. Z. Wang, Z. Y. Hou, Q. L. Zhang, R. L. Tian, and J. Z. Gu, Phys. Rev. C **91**, 017302 (2015).
[13] J. Dechargé, J.-F. Berger, K. Dietrich, and M. Weiss, Phys. Lett. B **451**, 275 (1999).
[14] A. V. Afanasjev and S. Frauendorf, Phys. Rev. C **71**, 024308 (2005).
[15] J. C. Pei, F. R. Xu, and P. D. Stevenson, Phys. Rev. C **71**, 034302 (2005).
[16] K. Dietrich and K. Pomorski, Phys. Rev. Lett. **80**, 37 (1998).
[17] T. Otsuka, T. Suzuki, R. Fujimoto, H. Grawe, and Y. Akaishi, Phys. Rev. Lett. **95**, 232502 (2005).
[18] B. A. Brown, T. Duguet, T. Otsuka, D. Abe, and T. Suzuki, Phys. Rev. C **74**, 061303 (2006).
[19] T. Otsuka, T. Matsuo, and D. Abe, Phys. Rev. Lett. **97**, 162501 (2006).
[20] G. Colò, H. Sagawa, S. Fracasso, and P. Bortignon, Phys. Lett. B **646**, 227 (2007).
[21] T. Lesinski, M. Bender, K. Bennaceur, T. Duguet, and J. Meyer, Phys. Rev. C **76**, 014312 (2007).
[22] H. Nakada, Phys. Rev. C **78**, 054301 (2008).
[23] W. H. Long, H. Sagawa, J. Meng, and N. Van Giai, Europhys. Lett. **82**, 12001 (2008).
[24] G. A. Lalazissis, S. Karatzikos, M. Serra, T. Otsuka, and P. Ring, Phys. Rev. C **80**, 041301 (2009).
[25] M. Anguiano, M. Grasso, G. Co', V. De Donno, and A. M. Lallena, Phys. Rev. C **86**, 054302 (2012).
[26] H. Sagawa and G. Colò, Prog. Part. Nucl. Phys. **76**, 76 (2014).
[27] L. J. Jiang, S. Yang, B. Y. Sun, W. H. Long, and H. Q. Gu, Phys. Rev. C **91**, 034326 (2015).
[28] L. J. Jiang, S. Yang, J. M. Dong, and W. H. Long, Phys. Rev. C **91**, 025802 (2015).
[29] J. J. Li, J. Margueron, W. H. Long, and N. Van Giai, Phys. Lett. B **753**, 97 (2016).
[30] J. D. Walecka, Ann. Phys. (N.Y.) **83**, 491 (1974).
[31] B. D. Serot and J. D. Walecka, Adv. Nucl. Phys. **16**, 1 (1986).
[32] P.-G. Reinhard, Rep. Prog. Phys. **52**, 439 (1989).
[33] Y. K. Gambhir, P. Ring, and A. Thimet, Ann. Phys. (N.Y.) **198**, 132 (1990).
[34] P. Ring, Prog. Part. Nucl. Phys. **37**, 193 (1996).
[35] M. Bender, P.-H. Heenen, and P.-G. Reinhard, Rev. Mod. Phys. **75**, 121 (2003).
[36] D. Vretenar, A. V. Afanasjev, G. A. Lalazissis, and P. Ring, Phys. Rep. **409**, 101 (2005).
[37] J. Meng, H. Toki, S. G. Zhou, S. Q. Zhang, W. H. Long, and L. S. Geng, Prog. Part. Nucl. Phys. **57**, 470 (2006).
[38] N. Paar, D. Vretenar, E. Khan, and G. Colò, Rep. Prog. Phys. **70**, 691 (2007).
[39] T. Nikšić, D. Vretenar, and P. Ring, Prog. Part. Nucl. Phys. **66**, 519 (2011).
[40] A. Bouyssy, S. Marcos, J. F. Mathiot, and N. Van Giai, Phys. Rev. Lett. **55**, 1731 (1985).
[41] A. Bouyssy, J.-F. Mathiot, N. Van Giai, and S. Marcos, Phys. Rev. C **36**, 380 (1987).
[42] R. Fritz, H. Müther, and R. Machleidt, Phys. Rev. Lett. **71**, 46 (1993).
[43] P. Bernardos, V. N. Fomenko, N. V. Giai, M. L. Quelle, S. Marcos, R. Niembro, and L. N. Savushkin, Phys. Rev. C **48**, 2665 (1993).
[44] H.-L. Shi, B.-Q. Chen, and Z.-Y. Ma, Phys. Rev. C **52**, 144 (1995).
[45] L. N. Savushkin, S. Marcos, M. L. Quelle, P. Bernardos, V. N. Fomenko, and R. Niembro, Phys. Rev. C **55**, 167 (1997).
[46] S. Marcos, L. N. Savushkin, V. N. Fomenko, M. López-Quelle, and R. Niembro, J. Phys. G: Nucl. Part. Phys. **30**, 703 (2004).
[47] W. H. Long, N. Van Giai, and J. Meng, Phys. Lett. B **640**, 150 (2006).

[48] W. H. Long, H. Sagawa, N. V. Giai, and J. Meng, Phys. Rev. C **76**, 034314 (2007).
[49] L. J. Wang, J. M. Dong, and W. H. Long, Phys. Rev. C **87**, 047301 (2013).
[50] W. H. Long, T. Nakatsukasa, H. Sagawa, J. Meng, H. Nakada, and Y. Zhang, Phys. Lett. B **680**, 428 (2009).
[51] J. J. Li, W. H. Long, J. Margueron, and N. Van Giai, Phys. Lett. B **732**, 169 (2014).
[52] H. Z. Liang, N. Van Giai, and J. Meng, Phys. Rev. Lett. **101**, 122502 (2008).
[53] H. Liang, N. V. Giai, and J. Meng, Phys. Rev. C **79**, 064316 (2009).
[54] H. Liang, P. Zhao, and J. Meng, Phys. Rev. C **85**, 064302 (2012).
[55] Z. M. Niu, Y. F. Niu, H. Z. Liang, W. H. Long, T. Nikšić *et al.*, Phys. Lett. B **723**, 172 (2013).
[56] A. Arima, M. Harvey, and K. Shimizu, Phys. Lett. B **30**, 517 (1969).
[57] K. T. Hecht and A. Adler, Nucl. Phys. A **137**, 129 (1969).
[58] A. Bohr, I. Hamamoto, and B. R. Mottelson, Phys. Scr. **26**, 267 (1982).
[59] F. S. Stephens, M. A. Deleplanque, J. E. Draper, R. M. Diamond, A. O. Macchiavelli *et al.*, Phys. Rev. Lett. **65**, 301 (1990).
[60] S. Marcos, L. N. Savushkin, M. López-Quelle, and P. Ring, Phys. Rev. C **62**, 054309 (2000).
[61] J. N. Ginocchio, Phys. Rep. **414**, 165 (2005).
[62] W. H. Long, H. Sagawa, J. Meng, and N. Van Giai, Phys. Lett. B **639**, 242 (2006).
[63] H. Liang, J. Meng, and S.-G. Zhou, Phys. Rep. **570**, 1 (2015).
[64] J. N. Ginocchio, Phys. Rev. Lett. **78**, 436 (1997).
[65] J. Meng, K. Sugawara-Tanabe, S. Yamaji, P. Ring, and A. Arima, Phys. Rev. C **58**, R628 (1998).
[66] P. Alberto, M. Fiolhais, M. Malheiro, A. Delfino, and M. Chiapparini, Phys. Rev. Lett. **86**, 5015 (2001).
[67] P. Alberto, M. Fiolhais, M. Malheiro, A. Delfino, and M. Chiapparini, Phys. Rev. C **65**, 034307 (2002).
[68] J. Meng, K. Sugawara-Tanabe, S. Yamaji, and A. Arima, Phys. Rev. C **59**, 154 (1999).
[69] O. Sorlin and M.-G. Porquet, Prog. Part. Nucl. Phys. **61**, 602 (2008).
[70] J. J. Li, J. Margueron, W. H. Long, and N. Van Giai, Phys. Rev. C **92**, 014302 (2015).
[71] W. H. Long, P. Ring, J. Meng, N. Van Giai, and C. A. Bertulani, Phys. Rev. C **81**, 031302(R) (2010).
[72] X. L. Lu, B. Y. Sun, and W. H. Long, Phys. Rev. C **87**, 034311 (2013).
[73] L. Geng, H. Toki, and J. Meng, Prog. Theor. Phys. **113**, 785 (2005).
[74] Q.-S. Zhang, Z.-M. Niu, Z.-P. Li, J.-M. Yao, and J. Meng, Front. Phys. **9**, 529 (2014).
[75] W. H. Long, P. Ring, N. Van Giai, and J. Meng, Phys. Rev. C **81**, 024308 (2010).
[76] J.-P. Ebran, E. Khan, D. Peña Arteaga, and D. Vretenar, Phys. Rev. C **83**, 064323 (2011).
[77] J. J. Li, Ph.D. thesis, Université Paris-Sud, 2015 (unpublished).
[78] J. F. Berger, M. Girod, and D. Gogny, Nucl. Phys. A **428**, 23 (1984).
[79] N. Tajima, P. Bonche, H. Flocard, P.-H. Heenen, and M. S. Weiss, Nucl. Phys. A **551**, 434 (1993).
[80] S.-G. Zhou, J. Meng, and P. Ring, Phys. Rev. C **68**, 034323 (2003).
[81] Y. Sugahara and H. Toki, Nucl. Phys. A **579**, 557 (1994).
[82] G. A. Lalazissis, T. Nikšić, D. Vretenar, and P. Ring, Phys. Rev. C **71**, 024312 (2005).
[83] L. J. Wang, B. Y. Sun, J. M. Dong, and W. H. Long, Phys. Rev. C **87**, 054331 (2013).
[84] S. E. Agbemava, A. V. Afanasjev, D. Ray, and P. Ring, Phys. Rev. C **89**, 054320 (2014).
[85] H. Grawe, K. Langanke, and G. Martínez-Pinedo, Rep. Prog. Phys. **70**, 1525 (2007).
[86] R. Hofstadter, Rev. Mod. Phys. **28**, 214 (1956).
[87] T. W. Donnelly and J. D. Walecka, Annu. Rev. Nucl. Part. Sci. **25**, 329 (1975).
[88] I. Angeli and K. P. Marinova, J. Phys. G: Nucl. Part. Phys. **42**, 055108 (2015).
[89] T. Otsuka and N. Fukunishi, Phys. Rep. **264**, 297 (1996).
[90] S. Hilaire and M. Girod, Eur. Phys. J. A **33**, 237 (2007).
[91] J. Erler, N. Birge, M. Kortelainen, W. Nazarewicz, E. Olsen *et al.*, Nature (London) **486**, 509 (2012).
[92] D. Rychel, H. J. Emrich, H. Miska, R. Gyufko, and C. A. Wiedner, Phys. Lett. B **130**, 5 (1983).
[93] S. Khan, T. Kihm, K. T. Knöpfle, G. Mairle, V. Bechtold *et al.*, Phys. Lett. B **156**, 155 (1985).
[94] J. M. Yao, H. Mei, and Z. P. Li, Phys. Lett. B **723**, 459 (2013).
[95] G. Burgunder, O. Sorlin, F. Nowacki, S. Giron, F. Hammache *et al.*, Phys. Rev. Lett. **112**, 042502 (2014).
[96] G. Audi, F. G. Kondev, M. Wang, B. Pfeiffer, X. Sun *et al.*, Chin. Phys. C **36**, 1157 (2012).
[97] H. De Vries, C. De Jager, and C. De Vries, At. Data Nucl. Data Tables **36**, 495 (1987).
[98] Y. Chu, Z. Ren, Z. Wang, and T. Dong, Phys. Rev. C **82**, 024320 (2010).
[99] L. Gaudefroy, O. Sorlin, D. Beaumel, Y. Blumenfeld, Z. Dombrádi *et al.*, Phys. Rev. Lett. **99**, 099202 (2007).
[100] B. Bastin, S. Grévy, D. Sohler, O. Sorlin, Z. Dombrádi *et al.*, Phys. Rev. Lett. **99**, 022503 (2007).
[101] A. J. C. Burghard, Ph.D. thesis, University of Amsterdam, 1989 (unpublished).
[102] X. Roca-Maza, M. Centelles, F. Salvat, and X. Viñas, Phys. Rev. C **78**, 044332 (2008).
[103] X. Roca-Maza, M. Centelles, F. Salvat, and X. Viñas, Phys. Rev. C **87**, 014304 (2013).
[104] T. W. Donnelly, J. Dubach, and I. Sick, Nucl. Phys. A **503**, 589 (1989).
[105] X. Roca-Maza, M. Centelles, X. Viñas, and M. Warda, Phys. Rev. Lett. **106**, 252501 (2011).
[106] P. G. Thirolf, B. V. Pritychenko, B. A. Brown, P. D. Cottle, M. Chromik *et al.*, Phys. Lett. B **485**, 16 (2000).
[107] M. Stanoiu, F. Azaiez, Z. Dombrádi, O. Sorlin, B. A. Brown *et al.*, Phys. Rev. C **69**, 034312 (2004).
[108] E. Becheva, Y. Blumenfeld, E. Khan, D. Beaumel, J. M. Daugas *et al.*, Phys. Rev. Lett. **96**, 012501 (2006).
[109] A. Ozawa, T. Kobayashi, T. Suzuki, K. Yoshida, and I. Tanihata, Phys. Rev. Lett. **84**, 5493 (2000).
[110] C. R. Hoffman, T. Baumann, D. Bazin, J. Brown, G. Christian *et al.*, Phys. Rev. Lett. **100**, 152502 (2008).
[111] K. Tshoo, Y. Satou, H. Bhang, S. Choi, T. Nakamura *et al.*, Phys. Rev. Lett. **109**, 022501 (2012).
[112] R. Kanungo, I. Tanihata, and A. Ozawa, Phys. Lett. B **528**, 58 (2002).

[113] K. Rutz, M. Bender, T. Bürvenich, T. Schilling, P.-G. Reinhard, J. A. Maruhn, and W. Greiner, Phys. Rev. C **56**, 238 (1997).
[114] W. Zhang, J. Meng, S. Zhang, L. Geng, and H. Toki, Nucl. Phys. A **753**, 106 (2005).
[115] S. E. Agbemava, A. V. Afanasjev, T. Nakatsukasa, and P. Ring, Phys. Rev. C **92**, 054310 (2015).
[116] J. Dechargé, J.-F. Berger, M. Girod, and K. Dietrich, Nucl. Phys. A **716**, 55 (2003).
[117] M. Bender, K. Rutz, P.-G. Reinhard, J. A. Maruhn, and W. Greiner, Phys. Rev. C **60**, 034304 (1999).
[118] J. Meng, Phys. Rev. C **57**, 1229 (1998).
[119] N. Sandulescu, P. Schuck, and X. Viñas, Phys. Rev. C **71**, 054303 (2005).
[120] S. Shen, H. Liang, P. Zhao, S. Zhang, and J. Meng, Phys. Rev. C **88**, 024311 (2013).
[121] M. López-Quelle, N. Van Giai, S. Marcos, and L. N. Savushkin, Phys. Rev. C **61**, 064321 (2000).
[122] X. Roca-Maza, X. Viñas, M. Centelles, P. Ring, and P. Schuck, Phys. Rev. C **84**, 054309 (2011).
[123] W. H. Long, J. Meng, N. Van Giai, and S.-G. Zhou, Phys. Rev. C **69**, 034319 (2004).
[124] M. Grasso and M. Anguiano, Phys. Rev. C **92**, 054316 (2015).